Tele-echography of Moving Organs Using an Impedance-controlled Telerobotic System

Mojtaba Sharifi [a,b,c,*], Hassan Salarieh [c], Saeed Behzadipour [c], Mahdi Tavakoli [b]

[a] *Department of Mechanical Engineering, Shiraz University, Shiraz, 71936, Iran*
[b] *Department of Electrical and Computer Engineering, University of Alberta, Edmonton, Alberta, T6G 1H9, Canada*
[c] *Department of Mechanical Engineering, Sharif University of Technology, Tehran, 11155-9567, Iran*

Abstract

A novel impedance-controlled teleoperation system is developed for robot-assisted tele-echography of moving organs such as heart, chest and breast during their natural motions (beating and/or breathing). The procedure of devising the two impedance models for the master and slave robots is developed such that (a) the slave robot holding the ultrasound (US) probe follows the master trajectory but complies with the oscillatory interaction force of the moving organ, and (b) the sonographer receives feedback from the non-oscillatory portion of the slave-organ interaction force via the master robot similar to the haptic feedback received in echography of a stationary organ. These goals are achieved via appropriate parameter adjustment in the desired impedance models without requiring any direct measurement and/or online prediction of the organ's motions. The stability and tracking convergence of the teleoperation system in the presence of communication delays and modeling uncertainties are proven in a Lyapunov-based framework. The performance of the proposed tele-echography system is evaluated experimentally using a master-slave telerobotic system, a US imaging system and a mechanical moving-organ simulator.

Keywords: Tele-echography, medical robots and systems, impedance adjustment, telerobotics, physical human-robot interaction.

1. Introduction

In recent years, remote diagnosis and health monitoring has drawn great attention due to the practical challenges associated with delivering health services to remote areas. Accordingly, telerobotic systems have been developed for different biomedical applications such as tele-surgery [1, 2], tele-rehabilitation [3, 4] and tele-echography [5, 6]. In a telerobotic system, the human operator applies forces to the master robot at the local site in order to control the position of the slave robot at the remote site which tracks the master robot's trajectory.

So far, some robot-assisted US imaging systems (e.g., [7, 8]) have been proposed for scanning the stationary tissues. In [9, 10], a force-based control strategy was employed for the robot to provide a specified interaction force between the US probe and the tissue while maintaining the contact. The telerobotic systems [5, 6, 11-18] have also been employed to perform remote ultrasound imaging using a slave robot based on the online motion measurement of the sonographer's hand interacting with the master robot. In these systems, position tracking controllers were implemented sometimes with reflecting the tissue force [5, 11, 14-16, 18] to the sonographer.

While the above-mentioned works have focused on stationary organs, the remote US imaging (tele-echography) of the moving tissues such as the human heart and/or chest with a telerobotic system has remained as one of the challenging and open issues in the field of medical robotics. The ultrasound imaging of the heart during its normal beating will be significantly useful in the beating-heart surgeries (such as catheter ablation and mitral valve repair) for online detection of the catheter and/or surgery instrument inside the heart. Moreover, the tele-echography of other moving tissues inside the chest (e.g., lung) or outside it (e.g., breast) during normal respiration is useful for the intraoperative evaluations.

Arresting the heart to perform a stationary surgery may have undesirable side effects due to the use of the heart–lung machine

for the circulation of blood and the ventilation of lungs. Also, after this operation, the surgeon attempts to restart the heart which may cause irregular heartbeats. Some other disadvantages of the arrested heart surgery are increasing the stroke risk [19] and long-time cognitive decline [20]. On the other hand, physical interaction with the heart as a moving organ is challenging due to its beating velocity and acceleration that are more than 210 mm/sec and 3800 mm/sec^2, respectively [21]. Accordingly, in some surgeries such as catheter ablation and mitral valve repair, the heart is allowed to beat freely during the surgery operation to wipe out the mentioned risks and side effects.

However, during these beating-heart surgeries, the online monitoring of the catheter and/or the surgical instruments' position inside the heart is a vital requirement. A method for screening the position of an instrument inside a tissue would be online ultrasound imaging. Moreover, the imaging of moving organs such as the beating-heart and chest (during the normal breathing) is helpful and has important information for *intraoperative* evaluation of dynamic moving structures. This condition would be achieved via a telerobotic system in which a slave robot has a compliant interaction with the moving tissue, and the sonographer performs the US imaging via a master robot without the requirement of synchronizing with the oscillatory motions of the tissue.

In the past decade, some control methods have been proposed for linear and nonlinear telerobotic systems [22-26] with the purpose of position and force tracking; however, they cannot be used in the tele-echography of a moving organ (e.g. the heart) which requires a motion or force compensation strategy in addition to a stable bilateral teleoperation.

Some control strategies [27-31] have been suggested for the compensation of the heart's physiological motion and synchronization of the robot with the heart using visual information and the predictive algorithms. In [32], the robot was synchronized with the heart using a high speed camera detecting target points. The Model Predictive Control (MPC) method was employed in [27, 29] to predict the heart motion (with a known constant heartbeat rate), and the Smith predictor and Kalman filter were suggested in [30] and [31], respectively. However, these position-based methods have some drawbacks such as: a) a vision device with artificial or natural landmarks inside the surgery environment is required, b) during the echography and/or surgery, the heart soft tissue deforms in physical interactions with the instrument that increases the error of the vision systems, c) the processing of some vision data is time-consuming and generate significant delays in addition to communication delays.

Some other control strategies [1, 33, 34] were presented based on the force data to overcome the above-mentioned disadvantages. In this context, the iterative learning control [35] and active observer (AOB) based force control [36] methods were used to compensate the physiological motion. The MPC method was also proposed as a linear predictive force controller [37] and its performance was compared with the AOB approach in [38]. Lastly, a cascade force controller [39] was presented via a combination of the MPC and AOB approaches to compensate physiological disturbances. Moreover, a force-based position tracking system [40, 41] was developed to apply a constant force on the heart's mitral valve using a catheter robotic system.

It should be mentioned that none of the previous vision/position-based or the force-based controllers for the beating-heart interaction was used for the tele-echography. Also, these controllers used predictive and/or observer-based methods or a combination of them while the convergence and robustness as well as the stability were not proved analytically. Moreover, the rate of disturbance observation and/or prediction should be significantly faster than the heart beat rate which is challenging to achieve in practice.

In this paper, a novel impedance-controlled telerobotic system is proposed and tested for tele-echography (remote ultrasound imaging). For the first time, the robotic tele-echography is investigated for imaging of moving organs (e.g. beating-heart and chest). To this end, the proposed control method employs the measured robot-tissue interaction forces but does not require any prediction, observation and/or learning of the organ's motion. In this bilateral telerobotic system, a virtual impedance model is implemented for the slave robot in order to comply with the natural force and/or disturbance of the moving tissue during the tracking of the master robot's trajectory. Moreover, the sonographer senses the tissue interaction force through the haptic feedback by implementing another impedance model for the master robot end-effector. The master impedance model can be adjusted such that the non-oscillatory part of the tissue force is provided for the sonographer (similar to a stationary tissue), which is useful for the tele-echography of beating-heart that has high-frequency oscillatory interaction forces. Under this condition, the sonographer's fatigue will decrease as he does not feel the high-frequency haptic force of the moving tissue during the imaging operation.

For these purposes, the structure and parameters of the master and slave impedance models are designed appropriately such that they have desired responses with respect to the interaction forces of the sonographer and tissue. Also, the bounded time delays were taken into account in the communication channels between the local sonographer site and the remote patient site. The impedance models are realized on a multi-DOF master and slave robotic system with modeling uncertainties employing a new nonlinear bilateral adaptive controller. Using the Lyapunov stability theorem, the proposed telerobotic ultrasound imaging system is guaranteed to be stable and robust against communication delays and the modeling uncertainties..

2. Impedance-controlled Telerobotic System with Communication Delays for Tele-echography

2.1. Signals in Delayed Communication Channels

The transmitted signals and imaging data with bounded time delays inside the communication channels are expressed in Fig. 1 for the presented robotic tele-echography system. As seen in this figure, the position $\mathbf{x}_m$, velocity $\dot{\mathbf{x}}_m$ and the sonographer-master interaction force $\mathbf{f}_{son}$ are transmitted from the local site to the remote slave-patient site via a communication channel with a time delay of T_1. On the other hand, the interaction force between the US probe (slave robot) and the moving tissue $\mathbf{f}_{tis}$ is transmitted back from the remote patient to the local sonographer. Also, the US data is transmitted from the US machine in the remote site to the sonographer. Moreover, the images of the patient's organ during the interaction with the US probe/slave robot are captured using a camera and provided online for the sonographer to perform the operation appropriately on the master robot. These signals and imaging data are transmitted from the remote to local site by the other communication channel that has a time delay of T_2.
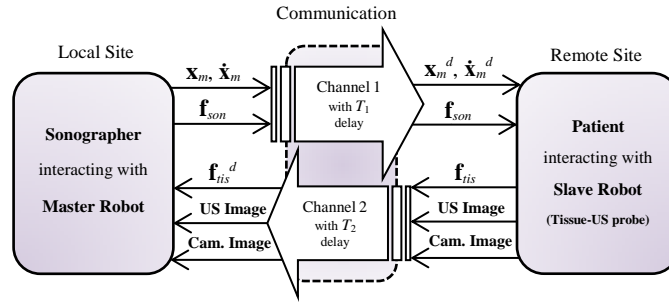

Fig. 1. The signals and imaging data transmitted via delayed communication channels.

The input and output signals of the communication channels are expressed in terms of time delays as

$$\mathbf{x}_m^d(t) = \mathbf{x}_m(t - T_1), \quad \dot{\mathbf{x}}_m^d(t) = \dot{\mathbf{x}}_m(t - T_1), \quad \mathbf{f}_{son}^d(t) = \mathbf{f}_{son}(t - T_1), \quad \mathbf{f}_{tis}^d(t) = \mathbf{f}_{tis}(t - T_2) \tag{1}$$

The position and velocity (trajectory) of the master/sonographer is scaled by η_p and the interaction force between the US probe and the moving organ is scaled by η_f before being used in the corresponding impedance model of the other robot:

$$\mathbf{x}_{m_{scaled}} = \eta_p \mathbf{x}_m, \quad \dot{\mathbf{x}}_{m_{scaled}} = \eta_p \dot{\mathbf{x}}_m, \quad \mathbf{f}_{tis_{scaled}} = \eta_f \mathbf{f}_{tis} \tag{2}$$

This feature is useful for scaling down or up the sonographer's trajectory for the slave robot (US probe), and the haptic force feedback of the tissue for the sonographer.

2.2. Master and Slave Impedance Models

Two reference impedance models are designed for the slave and master robots to realize telerobotic remote ultrasound imaging on moving tissues (e.g. beating-heart and/or chest) using a nonlinear bilateral controller.

The reference impedance model of the slave robot is defined as a dynamical relationship between the US probe-moving tissue interaction force $\mathbf{f}_{tis}$ and the desired slave deviation from the sonographer/master trajectory in Cartesian space as:

$$m_s \ddot{\tilde{\mathbf{x}}}_{imp_s} + c_s \dot{\tilde{\mathbf{x}}}_{imp_s} + k_s \tilde{\mathbf{x}}_{imp_s} = -\mathbf{f}_{tis} \tag{3}$$

where $\tilde{\mathbf{x}}_{imp_s} = \mathbf{x}_{imp_s} - \eta_p \mathbf{x}_m^d$ is the error of the slave impedance response (desired slave deviation) with respect to the scaled delayed master trajectory. k_s, c_s and m_s are the virtual stiffness, damping and mass parameters of the slave impedance model.

The reference impedance model of the master robot is also defined as a dynamics between the summation of the sonographer and the scaled delayed moving tissue forces, from one side, and the desired master response trajectory in Cartesian coordinates, from the other side, as:

$$m_m \ddot{\mathbf{x}}_{imp_m} + c_m \dot{\mathbf{x}}_{imp_m} + k_m \mathbf{x}_{imp_m} = \mathbf{f}_{son} - \eta_f \mathbf{f}_{tis}^d \tag{4}$$

where $\mathbf{x}_{imp_m}$ is the response position of the master impedance model. k_m, c_m and m_m are the virtual stiffness, damping and mass parameters of the master impedance model, respectively.

The concepts of the two defined impedance models (3) and (4) are schematically expressed in Fig. 2. The master impedance model (4) is perceived by the sonographer (as the haptic perception), and the slave impedance model (3) is the flexibility of slave robot with respect to the sonographer/master trajectory in response to the natural heart tissue forces ($\mathbf{f}_{tis}$). Also, a nonlinear bilateral adaptive controller is designed in Sec. 3 for tracking the impedance models (3) and (4) by the slave and master robots.

It should be mentioned as an important issue that both of the slave (3) and master (4) reference impedance models are stable second-order differential equations using positive impedance parameters. This stability characteristic of reference impedance models enhances the patient safety during the robotic US imaging.
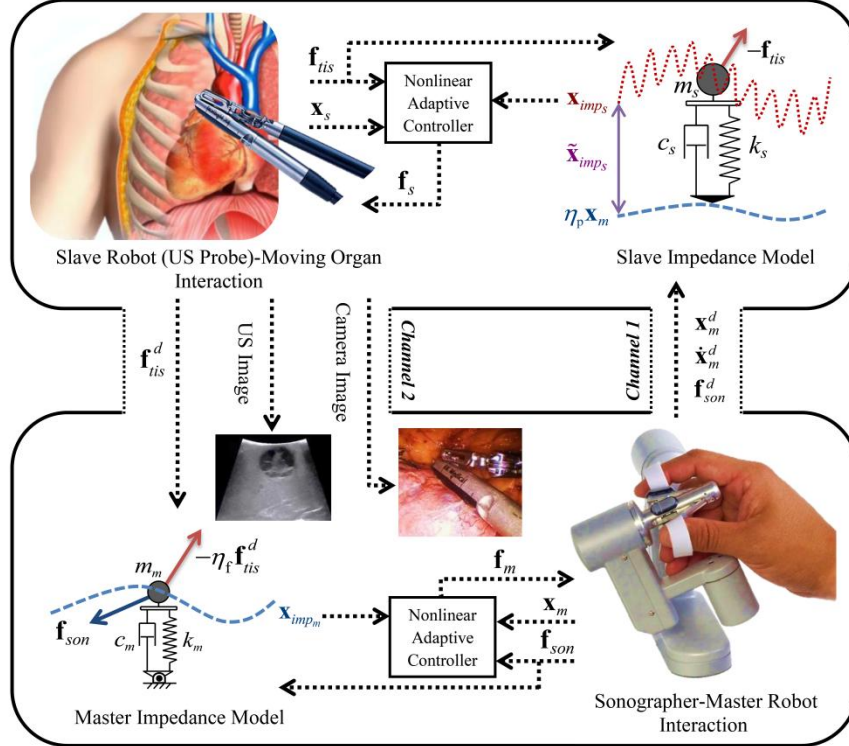

Fig. 2. The concepts of master and slave reference impedance models in the proposed telerobotic remote US imaging systems.

2.3. Adjustment of Slave Impedance Model

The slave impedance model (3) should be adjusted such that the slave robot complies with the physiological force and/or disturbance of the moving tissue during the tracking of the scaled delayed sonographer's hand/master robot trajectory. For this compliance behavior, the flexibility of the slave robot should be adjusted appropriately by using as small as needed parameters in the slave impedance model (3). In other words, the slave robot's flexibility and its deviation from the master trajectory ($\tilde{\mathbf{x}}_{imp_s} = \mathbf{x}_{imp_s} - \eta_p \mathbf{x}_m^d$) increase in response to the tissue force ($\mathbf{f}_{tis}$) by decreasing k_s, c_s and m_s in (3). Therefore, the slave robot's end-effector (i.e. US probe) has an oscillatory motion in response to the oscillatory portion of the moving tissue interaction force $\mathbf{f}_{tis}$.

Nevertheless, too small values of the slave impedance parameters (k_s, c_s and m_s) make the slave robot too flexible such that it cannot apply sufficient forces to the moving organ in order to have appropriate US probe-tissue contact. However, too large values of these impedance parameters cause a rigid (non-compliant) behavior for the US probe-tissue interaction. In this case, large forces are applied to the moving tissue. This implies a trade-off between the flexibility and force applying characteristics of the slave.

4

In this work, the damping ratio of the slave impedance model (3) as a second-order differential equation is set to $\zeta_s = c_s / 2\sqrt{m_s k_s} = 0.7$ such that it has a fast behavior with respect to the dimensionless time $\omega_{n_s} t$ (also with a small over shoot in response to the step forces). In addition, the natural frequency $\omega_{n_s} = \sqrt{k_s / m_s}$ (the cut-off frequency when $\zeta_s = 0.7$) of the slave impedance model (3) should be adjusted larger than the motion frequency range ω_{MT} of the moving tissue (e.g. for the beating-heart $\omega_{MT} \simeq 1 - 1.7$ Hz $= 6.28 - 10.68$ rad/sec, or for the breathing-chest $\omega_{MT} \simeq 0.2 - 0.5$ Hz $= 1.26 - 3.14$ rad/sec) to have agile flexibility in response to the slave-tissue interaction force.

Therefore, the procedure for choosing the slave impedance parameters (k_s, c_s and m_s) is as follows:

1) The stiffness parameter k_s is firstly set to an appropriate value based on the desired static relationship between the tissue interaction force and the slave robot's deviation from the master trajectory ($k_s = \mathbf{f}_{tis} / \tilde{\mathbf{X}}_{imp_s}$ based on (3) when $\mathbf{f}_{tis}$ and $\tilde{\mathbf{X}}_{imp_s}$ are assumed constant). The trade-off between the flexibility and force applying capacity of the slave robot should be considered, as discussed above.

2) In order to have a fast compliance with the oscillatory force and/or motion of the heart, the damping ratio of the slave impedance model is set to $\zeta_s = 0.7$ and its natural frequency is chosen larger than the moving tissue frequency range ($\omega_{n_m} > \omega_{MT}$).

3) The damping c_s and mass m_s parameters of the slave impedance model are obtained from the above adjusted quantities (k_s, $\zeta_s = c_s / 2\sqrt{m_s k_s}$ and $\omega_{n_s} = \sqrt{k_s / m_s}$).

4) The value of position scaling factor can be chosen less than one ($\eta_p < 1$) to enlarge the tissue dimensions perceived by the sonographer.

2.4. Adjustment of Master Impedance Model

In this bilateral telerobotic system, the master impedance model should provide the tissue interaction force for the sonographer as the haptic force feedback. Since $\mathbf{f}_{son}$ and $\mathbf{f}_{tis}^d$ in the right side of master impedance model (4) are bounded, $\mathbf{x}_{imp_m}$, $\dot{\mathbf{x}}_{imp_m}$ and $\ddot{\mathbf{x}}_{imp_m}$ in the left side of this equation are also bounded. Therefore, employing small values for the master impedance parameters k_m, c_m and m_m, the left side of Eq.(4) becomes small due to the boundedness of $\mathbf{x}_{imp_m}$, $\dot{\mathbf{x}}_{imp_m}$ and $\ddot{\mathbf{x}}_{imp_m}$. Accordingly, the right side of Eq. (4) is also small ($(\mathbf{f}_{son} - \eta_f \mathbf{f}_{tis}^d) \to 0$); therefore, the force reflecting performance is achieved.

Moreover, for the moving organs such as the beating-heart with the physiological high-frequency motions, the high-frequency portion ($\mathbf{f}_{tis_{HF}}$) of the total tissue force ($\mathbf{f}_{tis} = \mathbf{f}_{tis_{HF}} + \mathbf{f}_{tis_{LF}}$) is preferred not to be reflected to the sonographer hand. Because it would be challenging and exhausting for the sonographer to perform a US imaging operation with an oscillatory force, especially when the tissue force $\mathbf{f}_{tis}$ is scaled up in (4) by $\eta_f > 1$.

For this purpose, the second-order master impedance model (4) is designed such that its cut-off frequency ($\approx \omega_{n_m} = \sqrt{k_m / m_m}$) be smaller than the tissue motion's frequency range (ω_{MT}). The damping ratio of the master impedance model (4) is also adjusted at $\zeta_m = c_m / 2\sqrt{m_m k_m} = 0.7$ to have a fast response and a small overshoot, similar to the slave impedance adjustment in Sec. 2.3.

It should be taken into account that the desired master stiffness k_m in (4) should not be chosen too small because the amplitude of the high-frequency response of the master impedance model with respect to the high-frequency force of the tissue becomes large. In other words, $\mathbf{X}_{imp_{m_{HF}}} = -\eta_f \mathbf{F}_{tis_{HF}} / k_m$ increases by decreasing k_m based on Eq. (4). Therefore, there is a trade-off for the adjustment of the master stiffness such that choosing a too small value for k_m enhances the force reflection performance $(\mathbf{f}_{son} - \eta_f \mathbf{f}_{tis}^d) \to 0$ as mentioned before; however, it weakens the filtration of the high-frequency force of the moving tissue (in the sonographer's haptic feedback), and vice versa.

Accordingly, the adjustment procedure for the master impedance parameters (k_m, c_m and m_m) is summarized as:

1) The stiffness parameter k_m is firstly chosen small such that the static force reflection performance $(\mathbf{f}_{son} - \eta_f \mathbf{f}_{tis}^d) \to 0$ is approximately achieved under consideration of the high-frequency force filtration based on the above-mentioned trade-off.

2) The natural frequency is considered smaller than the tissue motion's frequency ($\omega_{n_m} < \omega_{MT}$) such that the high-frequency force of the beating heart is filtered as much as needed. However, too much small values of the natural frequency (ω_{n_m}) will cause the master impedance dynamics to be too slow and sluggish for the sonographer. The master damping ratio is also adjusted at $\zeta_m = 0.7$.

3) The damping c_m and mass m_m parameters are specified from the above chosen parameters (k_m, ζ_m and ω_{n_m}).

4) The force scaling factor can be chosen more than one ($\eta_f > 1$) to enlarge the tissue haptic force feedback $\mathbf{f}_{tis}$ provided for the sonographer during the US imaging. In this condition, the sonographer becomes more sensitive with respect to forces applied to the tissue (e.g. heart).

3. Bilateral Control of a Master-Slave Telerobotic System

3.1. Nonlinear Dynamics of Multi-DOF Telerobotic System

The nonlinear model of a multi-DOF telerobotic system with modeling uncertainties is expressed in the Cartesian space for the master and slave robots' end-effectors [42, 43]:

$$\mathbf{M}_{\mathbf{x},m}(\mathbf{q}_m)\ddot{\mathbf{x}}_m + \mathbf{C}_{\mathbf{x},m}(\mathbf{q}_m,\dot{\mathbf{q}}_m)\dot{\mathbf{x}}_m + \mathbf{G}_{\mathbf{x},m}(\mathbf{q}_m) + \mathbf{F}_{\mathbf{x},m}(\dot{\mathbf{q}}_m) = \mathbf{f}_m + \mathbf{f}_{son} \tag{5}$$

$$\mathbf{M}_{\mathbf{x},s}(\mathbf{q}_s)\ddot{\mathbf{x}}_s + \mathbf{C}_{\mathbf{x},s}(\mathbf{q}_s,\dot{\mathbf{q}}_s)\dot{\mathbf{x}}_s + \mathbf{G}_{\mathbf{x},s}(\mathbf{q}_s) + \mathbf{F}_{\mathbf{x},s}(\dot{\mathbf{q}}_s) = \mathbf{f}_s - \mathbf{f}_{tis} \tag{6}$$

where $\mathbf{q}_m$ and $\mathbf{q}_s$ are the joint angles, and $\mathbf{x}_m$ and $\mathbf{x}_s$ are the Cartesian end-effector positions of the master and slave robots, respectively. Also, $\mathbf{M}_{\mathbf{x},m}(\mathbf{q}_m)$ and $\mathbf{M}_{\mathbf{x},s}(\mathbf{q}_s)$ are the inertia/mass matrices, $\mathbf{C}_{\mathbf{x},m}(\mathbf{q}_m,\dot{\mathbf{q}}_m)$ and $\mathbf{C}_{\mathbf{x},s}(\mathbf{q}_s,\dot{\mathbf{q}}_s)$ include the centrifugal and Coriolis terms, $\mathbf{G}_{\mathbf{x},m}(\mathbf{q}_m)$ and $\mathbf{G}_{\mathbf{x},s}(\mathbf{q}_s)$ are the gravity terms, $\mathbf{F}_{\mathbf{x},m}(\dot{\mathbf{q}}_m)$ and $\mathbf{F}_{\mathbf{x},s}(\dot{\mathbf{q}}_s)$ are the friction torques, and $\mathbf{f}_m$ and $\mathbf{f}_s$ are the control torques (produced by the actuators) of the master and the slave robots, respectively. Moreover, $\mathbf{f}_{son}$ is the interaction force that the sonographer applies to the master robot end-effector and $\mathbf{f}_{tis}$ is the interaction force that the slave robot applies to the remote patient organ (moving tissue).

Using the subscript $i = m$ for the master and $i = s$ for the slave, kinematic transformations between the joint space and the Cartesian one for each robot are presented as

$$\mathbf{x}_i = \Omega_i(\mathbf{q}_i), \quad \dot{\mathbf{x}}_i = \mathbf{J}_i(\mathbf{q}_i)\dot{\mathbf{q}}_i, \quad \ddot{\mathbf{x}}_i = \mathbf{J}_i(\mathbf{q}_i)\ddot{\mathbf{q}}_i + \dot{\mathbf{J}}_i(\mathbf{q}_i)\dot{\mathbf{q}}_i \tag{7}$$

where $\mathbf{J}_i(\mathbf{q}_i) = d\Omega_i(\mathbf{q}_i)/d\mathbf{q}_i$ is the Jacobian matrix. The matrices of dynamic models in (5) and (6) have the following properties [24, 43, 44]:

- The left side of (5) and (6) is linearly parameterized as

$$\mathbf{M}_{\mathbf{x},i}(\mathbf{q}_i)\boldsymbol{\psi}_{1,i} + \mathbf{C}_{\mathbf{x},i}(\mathbf{q}_i,\dot{\mathbf{q}}_i)\boldsymbol{\psi}_{2,i} + \mathbf{G}_{\mathbf{x},i}(\mathbf{q}_i) + \mathbf{F}_{\mathbf{x},i}(\dot{\mathbf{q}}_i) = \mathbf{Y}_{\mathbf{x},i}(\boldsymbol{\psi}_{1,i}, \boldsymbol{\psi}_{2,i}, \mathbf{q}_i, \dot{\mathbf{q}}_i)\boldsymbol{\beta}_{\mathbf{x},i} \tag{8}$$

where $\boldsymbol{\beta}_{\mathbf{x},i}$ is the vector of unknown parameters of each robot. The regressor matrix $\mathbf{Y}_{\mathbf{x},i}$ includes known functions [43] in terms of the vectors $\boldsymbol{\psi}_{1,i}$ and $\boldsymbol{\psi}_{2,i}$ which will be defined in the next section.

- The inertia matrix $\mathbf{M}_{\mathbf{x},i}(\mathbf{q}_i)$ is symmetric positive definite and the matrix $\dot{\mathbf{M}}_{\mathbf{x},i}(\mathbf{q}_i) - 2\mathbf{C}_{\mathbf{x},i}(\mathbf{q}_i,\dot{\mathbf{q}}_i)$ is skew symmetric.

3.2. Nonlinear Adaptive Control Laws for Tracking of Impedance Responses

Responses of the two reference impedance models (3) and (4) defined in Sec. 2 should be tracked by the multi-DOF slave and master robots, respectively, which are considered to have modeling uncertainties. Therefore, two nonlinear adaptive control laws are designed for the robots for tracking their corresponding impedance responses in the presence of uncertainties and communication delays. For this purpose, the master and slave sliding surfaces are designed as

$$\mathbf{\epsilon}_m = \dot{\tilde{\mathbf{x}}}_m + \rho_{1,m}\tilde{\mathbf{x}}_m + \rho_{2,m}\int_0^t \tilde{\mathbf{x}}_m \, dt \, , \qquad \mathbf{\epsilon}_s = \dot{\tilde{\mathbf{x}}}_s + \rho_{1,s}\tilde{\mathbf{x}}_s + \rho_{2,s}\int_0^t \tilde{\mathbf{x}}_s \, dt \tag{9}$$

where $\tilde{\mathbf{x}}_m = \mathbf{x}_m - \mathbf{x}_{imp_m}$ and $\tilde{\mathbf{x}}_s = \mathbf{x}_s - \mathbf{x}_{imp_s}$ are the position tracking errors of the master and slave robots with respect to the responses of their impedance models (4) and (3), respectively. Also, $\rho_{1,m}$, $\rho_{2,m}$, $\rho_{1,s}$ and $\rho_{2,s}$ are positive constant parameters which provide the stability of the sliding surfaces (i.e. $\tilde{\mathbf{x}}_i \to 0$ as $\mathbf{\epsilon}_i \to 0$). The reference velocities for the master and slave are defined based on (9) as

$$\dot{\mathbf{x}}_{ref,m} = \dot{\mathbf{x}}_{imp_m} - \rho_{1,m}\tilde{\mathbf{x}}_m - \rho_{2,m}\int_0^t \tilde{\mathbf{x}}_m \, dt \, , \qquad \dot{\mathbf{x}}_{ref,s} = \dot{\mathbf{x}}_{imp_s} - \rho_{1,s}\tilde{\mathbf{x}}_s - \rho_{2,s}\int_0^t \tilde{\mathbf{x}}_s \, dt \tag{10}$$

such that the sliding surfaces (9) can be rewritten as $\mathbf{\epsilon}_m = \dot{\mathbf{x}}_m - \dot{\mathbf{x}}_{ref,m}$ and $\mathbf{\epsilon}_s = \dot{\mathbf{x}}_s - \dot{\mathbf{x}}_{ref,s}$. Now, the nonlinear bilateral adaptive control laws for the master and slave robot's end-effectors are defined as

$$\mathbf{f}_m = -\rho_{3,m}\hat{\mathbf{M}}_{\mathbf{x},m}(\mathbf{q}_m)\mathbf{\epsilon}_m + \hat{\mathbf{M}}_{\mathbf{x},m}(\mathbf{q}_m)\ddot{\mathbf{x}}_{ref,m} + \hat{\mathbf{C}}_{\mathbf{x},m}(\mathbf{q}_m,\dot{\mathbf{q}}_m)\dot{\mathbf{x}}_{ref,m} + \hat{\mathbf{G}}_{\mathbf{x},m}(\mathbf{q}_m) + \hat{\mathbf{F}}_{\mathbf{x},m}(\dot{\mathbf{q}}_m) - \mathbf{f}_{son} \tag{11}$$

$$\mathbf{f}_s = -\rho_{3,s}\hat{\mathbf{M}}_{\mathbf{x},s}(\mathbf{q}_s)\mathbf{\epsilon}_s + \hat{\mathbf{M}}_{\mathbf{x},s}(\mathbf{q}_s)\ddot{\mathbf{x}}_{ref,s} - \rho_{4,s}\,\mathrm{sgn}(\mathbf{\epsilon}_s) + \hat{\mathbf{C}}_{\mathbf{x},s}(\mathbf{q}_s,\dot{\mathbf{q}}_s)\dot{\mathbf{x}}_{ref,s} + \hat{\mathbf{G}}_{\mathbf{x},s}(\mathbf{q}_s) + \hat{\mathbf{F}}_{\mathbf{x},s}(\dot{\mathbf{q}}_s) + \mathbf{f}_{tis} \tag{12}$$

The accent $\wedge$ denotes the estimated and/or updated values of matrices, vectors and scalars. $\rho_{4,s}$ in (12) is a positive constant gain. It should be mentioned that the position $\mathbf{x}_m^d$, velocity $\dot{\mathbf{x}}_m^d$ and acceleration $\ddot{\mathbf{x}}_m^d$ of the master robot are required to obtain the desired slave response as $\mathbf{x}_{imp_s} = \mathbf{x}_m^d + \tilde{\mathbf{x}}_{imp_s}$, $\dot{\mathbf{x}}_{imp_s} = \dot{\mathbf{x}}_m^d + \dot{\tilde{\mathbf{x}}}_{imp_s}$ and $\ddot{\mathbf{x}}_{imp_s} = \ddot{\mathbf{x}}_m^d + \ddot{\tilde{\mathbf{x}}}_{imp_s}$; these are used in the salve control law (12), which involves $\mathbf{\epsilon}_s$, $\dot{\mathbf{x}}_{ref,s}$ and $\ddot{\mathbf{x}}_{ref,s}$. Moreover, since the measurement of the master robot acceleration $\ddot{\mathbf{x}}_m^d$ is prone to noise, it can be estimated with good accuracy when the master robot mimics its reference impedance model (4) as expressed below. The delayed master robot acceleration ($\ddot{\mathbf{x}}_m^d$) is estimated using Eq. (4) considering T_1 time delay for all signals as

$$\hat{\ddot{\mathbf{x}}}_m^d \simeq m_m^{-1}\left(\mathbf{f}_{son}^d - \eta_{\mathrm{f}}\mathbf{f}_{tis}^{dd}\right) - m_m^{-1} c_m \dot{\mathbf{x}}_{imp_m}^d - m_m^{-1} k_m \mathbf{x}_{imp_m}^d \tag{13}$$

where $\mathbf{f}_{tis}^{dd}(t) = \mathbf{f}_{tis}^d(t-T_1) = \mathbf{f}_{tis}(t-T_1-T_2)$ has $T_1 + T_2$ time delay, and other delayed signals in (13) with one superscript "d" have only T_1 time delay. Using this estimation, $\ddot{\mathbf{x}}_{imp_s} = \ddot{\mathbf{x}}_m^d + \ddot{\tilde{\mathbf{x}}}_{imp_s}$ is replaced by $\hat{\ddot{\mathbf{x}}}_{imp_s} = \hat{\ddot{\mathbf{x}}}_m^d + \ddot{\tilde{\mathbf{x}}}_{imp_s} = \ddot{\mathbf{x}}_m^d + \Delta\ddot{\mathbf{x}}_m^d + \ddot{\tilde{\mathbf{x}}}_{imp_s} = \ddot{\mathbf{x}}_{imp_s} + \Delta\ddot{\mathbf{x}}_m^d$ in $\ddot{\mathbf{x}}_{ref,s}$, which is used in the salve control law (12). The term $-\rho_{4,s}\,\mathrm{sgn}(\mathbf{\epsilon}_s)$ in Eq. (12) also provides the robustness of the system against the bounded estimation error of the master robot's acceleration ($\Delta\ddot{\mathbf{x}}_m^d = \hat{\ddot{\mathbf{x}}}_m^d - \ddot{\mathbf{x}}_m^d$). It is worth noting that the acceleration should be measured and used in the previous nonlinear bilateral adaptive controllers [24, 45] for multi-DOF teleoperation systems; however, it can be estimated accurately in this proposed impedance-based controller.

Based on the mentioned robots' property in Sec. 3.1, one can write (11) and (12) using a linear parameterization:

$$\mathbf{f}_m = \mathbf{Y}_{\mathbf{x},m}\hat{\mathbf{\beta}}_{\mathbf{x},m} - \mathbf{f}_{son} \, , \qquad \mathbf{f}_s = \mathbf{Y}_{\mathbf{x},s}\hat{\mathbf{\beta}}_{\mathbf{x},s} + \mathbf{f}_{tis} \tag{14}$$

where $\mathbf{Y}_{\mathbf{x},m}$ and $\mathbf{Y}_{\mathbf{x},s}$ are determined based on (8) in terms of the following known vectors:

$$\mathbf{\psi}_{1,m} = -\rho_{3,m}\,\mathbf{\epsilon}_m + \ddot{\mathbf{x}}_{ref,m}, \quad \mathbf{\psi}_{2,m} = \dot{\mathbf{x}}_{ref,m}, \quad \mathbf{\psi}_{1,s} = -\rho_{3,s}\,\mathbf{\epsilon}_s + \ddot{\mathbf{x}}_{ref,s}, \quad \mathbf{\psi}_{2,s} = \dot{\mathbf{x}}_{ref,s} \tag{15}$$

The closed-loop dynamics of the master and slave using the presented nonlinear bilateral adaptive controller is obtained by substitution of the control laws (11) and (12) or (14) in the end-effector dynamics (5) and (6) of the telerobotic system, which

concludes as the following equations:

$$\mathbf{M}_{\mathbf{x},m}(\dot{\boldsymbol{\varepsilon}}_m + \rho_{3,m}\boldsymbol{\varepsilon}_m) + \mathbf{C}_{\mathbf{x},m}\boldsymbol{\varepsilon}_m = \mathbf{Y}_{\mathbf{x},m}\tilde{\boldsymbol{\beta}}_{\mathbf{x},m} \tag{16}$$

$$\mathbf{M}_{\mathbf{x},s}(\dot{\boldsymbol{\varepsilon}}_s + \rho_{3,s}\boldsymbol{\varepsilon}_s) + \mathbf{C}_{\mathbf{x},s}\boldsymbol{\varepsilon}_s - \eta_{\mathrm{p}}\mathbf{M}_{\mathbf{x},s}\Delta\ddot{\mathbf{x}}_m^d + \rho_{4,s}\,\mathrm{sgn}(\boldsymbol{\varepsilon}_s) = \mathbf{Y}_{\mathbf{x},s}\tilde{\boldsymbol{\beta}}_{\mathbf{x},s} \tag{17}$$

where $\mathbf{Y}_{\mathbf{x},m}$ and $\mathbf{Y}_{\mathbf{x},s}$ are the regressor matrices defined in (8) in terms of $\boldsymbol{\psi}_{1,m}$, $\boldsymbol{\psi}_{1,s}$, $\boldsymbol{\psi}_{2,m}$, and $\boldsymbol{\psi}_{2,s}$ determined in (15). $\tilde{\boldsymbol{\beta}}_{\mathbf{x},m} = \hat{\boldsymbol{\beta}}_{\mathbf{x},m} - \boldsymbol{\beta}_{\mathbf{x},m}$ and $\tilde{\boldsymbol{\beta}}_{\mathbf{x},s} = \hat{\boldsymbol{\beta}}_{\mathbf{x},s} - \boldsymbol{\beta}_{\mathbf{x},s}$ are the estimation errors of master and slave dynamic parameters, respectively. $\Delta\ddot{\mathbf{x}}_m^d = \hat{\ddot{\mathbf{x}}}_m^d - \ddot{\mathbf{x}}_m^d$ is also the estimation error of the master robot's acceleration.

4. Stability and Convergence Proof in Presence of Time Delays and Modeling Uncertainties

In this section, the stability of the proposed telerobotic ultrasound imaging system in the presence of communication delays and modeling uncertainties is investigated. Moreover, the tracking convergence of the master and slave robots' trajectories to their desired impedance responses ($\mathbf{x}_m \to \mathbf{x}_{imp_m}$ and $\mathbf{x}_s \to \mathbf{x}_{imp_s}$) is proven. For these purposes, a positive definite Lyapunov function is introduced as

$$V(t) = \frac{1}{2}\left(\boldsymbol{\varepsilon}_m^T \mathbf{M}_{\mathbf{x},m}\boldsymbol{\varepsilon}_m + \tilde{\boldsymbol{\beta}}_{\mathbf{x},m}^T \mathbf{W}_m^{-1}\tilde{\boldsymbol{\beta}}_{\mathbf{x},m} + \boldsymbol{\varepsilon}_s^T \mathbf{M}_{\mathbf{x},s}\boldsymbol{\varepsilon}_s + \tilde{\boldsymbol{\beta}}_{\mathbf{x},s}^T \mathbf{W}_s^{-1}\tilde{\boldsymbol{\beta}}_{\mathbf{x},s}\right) \tag{18}$$

where the inertia matrices $\mathbf{M}_{\mathbf{x},m}$ and $\mathbf{M}_{\mathbf{x},s}$ and the constant matrices $\mathbf{W}_m$ and $\mathbf{W}_s$ are positive definite. Now, the first time derivative of Lyapunov function (18) is found as

$$\dot{V}(t) = (1/2)\boldsymbol{\varepsilon}_m^T \dot{\mathbf{M}}_{\mathbf{x},m}\boldsymbol{\varepsilon}_m + \boldsymbol{\varepsilon}_m^T \mathbf{M}_{\mathbf{x},m}\dot{\boldsymbol{\varepsilon}}_m + \dot{\hat{\boldsymbol{\beta}}}_{\mathbf{x},m}^T \mathbf{W}_m^{-1}\tilde{\boldsymbol{\beta}}_{\mathbf{x},m} + (1/2)\boldsymbol{\varepsilon}_s^T \dot{\mathbf{M}}_{\mathbf{x},s}\boldsymbol{\varepsilon}_s + \boldsymbol{\varepsilon}_s^T \mathbf{M}_{\mathbf{x},s}\dot{\boldsymbol{\varepsilon}}_s + \dot{\hat{\boldsymbol{\beta}}}_{\mathbf{x},s}^T \mathbf{W}_s^{-1}\tilde{\boldsymbol{\beta}}_{\mathbf{x},s} \tag{19}$$

where $\dot{\hat{\boldsymbol{\beta}}}_{\mathbf{x},i} = \dot{\tilde{\boldsymbol{\beta}}}_{\mathbf{x},i}$ because $\hat{\boldsymbol{\beta}}_{\mathbf{x},i} = \tilde{\boldsymbol{\beta}}_{\mathbf{x},i} + \boldsymbol{\beta}_{\mathbf{x},i}$ and the actual parameters are constant ($\dot{\boldsymbol{\beta}}_{\mathbf{x},i} = 0$). Employing $\mathbf{M}_{\mathbf{x},m}\dot{\boldsymbol{\varepsilon}}_m$ and $\mathbf{M}_{\mathbf{x},s}\dot{\boldsymbol{\varepsilon}}_s$ from the closed-loop dynamics (16) and (17) and based on the property of the robot manipulators' dynamics (introduced in Sec. 3.1 as $\dot{\mathbf{M}}_{\mathbf{x},i} - 2\mathbf{C}_{\mathbf{x},i}$ is skew symmetric), Eq. (19) is obtained as

$$\begin{aligned}\dot{V}(t) = &- \rho_{3,m}\boldsymbol{\varepsilon}_m^T \mathbf{M}_{\mathbf{x},m}\boldsymbol{\varepsilon}_m + \boldsymbol{\varepsilon}_m^T \mathbf{Y}_{\mathbf{x},m}\tilde{\boldsymbol{\beta}}_{\mathbf{x},m} + \dot{\hat{\boldsymbol{\beta}}}_{\mathbf{x},m}^T \mathbf{W}_m^{-1}\tilde{\boldsymbol{\beta}}_{\mathbf{x},m} \\ &- \rho_{3,s}\boldsymbol{\varepsilon}_s^T \mathbf{M}_{\mathbf{x},s}\boldsymbol{\varepsilon}_s + \boldsymbol{\varepsilon}_s^T\left(\eta_{\mathrm{p}}\mathbf{M}_{\mathbf{x},s}\Delta\ddot{\mathbf{x}}_m^d - \rho_{4,s}\,\mathrm{sgn}(\boldsymbol{\varepsilon}_s)\right) + \boldsymbol{\varepsilon}_s^T \mathbf{Y}_{\mathbf{x},s}\tilde{\boldsymbol{\beta}}_{\mathbf{x},s} + \dot{\hat{\boldsymbol{\beta}}}_{\mathbf{x},s}^T \mathbf{W}_s^{-1}\tilde{\boldsymbol{\beta}}_{\mathbf{x},s}\end{aligned} \tag{20}$$

The nonlinear adaptation laws for updating the estimated parameters of the telerobotic system are defined for the master and slave as

$$\dot{\hat{\boldsymbol{\beta}}}_{\mathbf{x},m} = -\mathbf{W}_m^T \mathbf{Y}_{\mathbf{x},m}^T \boldsymbol{\varepsilon}_m \;,\quad \dot{\hat{\boldsymbol{\beta}}}_{\mathbf{x},s} = -\mathbf{W}_s^T \mathbf{Y}_{\mathbf{x},s}^T \boldsymbol{\varepsilon}_s \tag{21}$$

such that the terms in (20) that include $\tilde{\boldsymbol{\beta}}_{\mathbf{q},m}$ and $\tilde{\boldsymbol{\beta}}_{\mathbf{q},s}$ are cancelled. As a result, the Lyapunov function's time derivative (21) is simplified to:

$$\dot{V}(t) = -\rho_{3,m}\boldsymbol{\varepsilon}_m^T \mathbf{M}_{\mathbf{x},m}\boldsymbol{\varepsilon}_m - \rho_{3,s}\boldsymbol{\varepsilon}_s^T \mathbf{M}_{\mathbf{x},s}\boldsymbol{\varepsilon}_s + \boldsymbol{\varepsilon}_s^T\left(\eta_{\mathrm{p}}\mathbf{M}_{\mathbf{x},s}\Delta\ddot{\mathbf{x}}_m^d - \rho_{4,s}\,\mathrm{sgn}(\boldsymbol{\varepsilon}_s)\right) \tag{22}$$

Note that $\dot{\mathbf{x}}_{imp_m}$ and $\mathbf{x}_{imp_m}$ are bounded as the response of the stable master impedance model (4) with bounded inputs (bounded interaction forces $\mathbf{f}_{son}$ and $\mathbf{f}_{tis}$), which implies the boundedness of $\hat{\ddot{\mathbf{x}}}_m$ obtained from (13). Moreover, it is reasonable that the master acceleration $\ddot{\mathbf{x}}_m$ is bounded because the master robot (5) is a physical system (with a second-order differential equation) having bounded input forces $\mathbf{f}_{son}$ and $\mathbf{f}_m$. Therefore, the estimation error of the master robot's acceleration ($\Delta\ddot{\mathbf{x}}_m^d = \hat{\ddot{\mathbf{x}}}_m^d - \ddot{\mathbf{x}}_m^d$) in Eq. (22) is bounded. Accordingly, the constant gain $\rho_{4,s}$ is adjusted such that the robustness against the bounded acceleration estimation error ($\Delta\ddot{\mathbf{x}}_m^d$) is guaranteed by satisfying the following inequality:

$$\rho_{4,s} \geq \eta_p \parallel \mathbf{M}_{\mathbf{x},s} \Delta \ddot{\mathbf{x}}_m^d \parallel_\infty \tag{23}$$

Note that the actual salve inertia matrix $\mathbf{M}_{\mathbf{x},s}$ is uncertain in this bilateral adaptive controller, and the bounded acceleration estimation error $\Delta \ddot{\mathbf{x}}_m^d$ is also unknown. However, $\rho_{4,s}$ should be chosen larger than the maximum value of $\eta_p \parallel \mathbf{M}_{\mathbf{x},s} \Delta \ddot{\mathbf{x}}_m^d \parallel_\infty$ based on (23) to ensure robust stability against acceleration estimation error. According to Eqs. (22) and (23), the time derivative of the Lyapunov function is finally obtained as

$$\dot{V}(t) \leq -\rho_{3,m} \boldsymbol{\varepsilon}_m^T \mathbf{M}_{\mathbf{x},m} \boldsymbol{\varepsilon}_m - \rho_{3,s} \boldsymbol{\varepsilon}_s^T \mathbf{M}_{\mathbf{x},s} \boldsymbol{\varepsilon}_s \tag{24}$$

Since the Lyapunov function (18) is positive definite ($V(t) > 0$) and its first time derivative (24) is negative semi-definite ($\dot{V}(t) \leq 0$), it can be shown using the Barbalat's lemma [43] that $\lim_{t \to \infty} \dot{V}(t) = 0$. Thus, since $\rho_{3,m} > 0$, $\rho_{3,s} > 0$, $\boldsymbol{\varepsilon}_m^T \mathbf{M}_{\mathbf{x},m} \boldsymbol{\varepsilon}_m \geq 0$ and $\boldsymbol{\varepsilon}_s^T \mathbf{M}_{\mathbf{x},s} \boldsymbol{\varepsilon}_s \geq 0$, Eq. (24) implies the convergence to sliding surfaces $\boldsymbol{\varepsilon}_m = 0$ and $\boldsymbol{\varepsilon}_s = 0$ as $t \to \infty$. In addition, it is concluded from Eq. (18) that the estimation errors $\tilde{\boldsymbol{\beta}}_{\mathbf{x},m}$ and $\tilde{\boldsymbol{\beta}}_{\mathbf{x},s}$ of the system parameters remain bounded due to the convergence of $\boldsymbol{\varepsilon}_m \to 0$ and $\boldsymbol{\varepsilon}_s \to 0$ and the boundedness of $V(t)$.

According to the stable dynamics of the sliding surfaces $\boldsymbol{\varepsilon}_m$ and $\boldsymbol{\varepsilon}_s$ in (9), the convergence of the master and slave tracking errors to zero $\tilde{\mathbf{x}}_m \to 0$ and $\tilde{\mathbf{x}}_s \to 0$ (on the surfaces of $\boldsymbol{\varepsilon}_m = 0$ and $\boldsymbol{\varepsilon}_s = 0$) are guaranteed. As a result, the proposed bilateral impedance-based control strategy ensures that the master and slave robots track their corresponding impedance models' responses, i.e. $\mathbf{x}_m \to \mathbf{x}_{imp_m}$ and $\mathbf{x}_s \to \mathbf{x}_{imp_s}$ in the presence of parametric uncertainties and communication delays. It should be mentioned that the tracked slave impedance response is defined in terms of the delayed master trajectory ($\mathbf{x}_m^d$) as $\mathbf{x}_{imp_s} = \eta_p \mathbf{x}_m^d + \tilde{\mathbf{x}}_{imp_s}$ where $\tilde{\mathbf{x}}_{imp_s}$ is the response of (3). Also, the tracked master impedance response $\mathbf{x}_{imp_m}$ is obtained from (4) as the response of the delayed moving tissue $\mathbf{f}_{tis}^d$ and the sonographer's $\mathbf{f}_{son}$ forces.

5. Experimental Evaluations

In this section, the proposed bilateral impedance-based control strategy is evaluated experimentally for the tele-echography of moving organs employing a multi-DOF telerobotic system. Moving organs with different motion rates such as the beating-heart frequency and the breathing frequency of the chest are included.

5.1. Telerobotic and Ultrasound Setup

A Phantom Premium 1.5A robot (Geomagic Inc., Wilmington, MA, USA) with three DOFs (revolute joints) and the Quanser robot (Quanser Consulting Inc., Markham, ON, Canada) with two DOFs (revolute joints) are used as the master and slave, respectively (Fig. 3). The workspace of the slave (Quanser) robot is a subset of the $x - y$ plane and the master (Phantom Premium) robot is controlled to move in the same 2D space, as shown in Fig. 3. The kinematics and dynamics of the Phantom and Quanser robots were presented comprehensively in [46] and [47, 48], respectively, and not repeated here for the sake of brevity.

The applied interaction forces of the sonographer and the moving organ are measured by the 6-axis JR3 50M31 force/torque sensor (JR3 Inc.,Woodland, CA, USA) and the ATI Gamma force/torque sensor (ATI Industrial Automation, Apex, NC, USA) respectively attached to the Phantom Premium and Quanser robots' end-effectors. The QUARC software (Quanser Consulting Inc., Markham, ON, Canada) is employed as a real-time control environment to implement the proposed controller with a $1\,k\mathrm{Hz}$ loop frequency.

A Sonix Touch ultrasound (US) imaging machine (Ultrasonix, Richmond, CA, USA) with a 4DL14-5/38 ultrasound probe is used in the experiments (Fig. 3). The two dimensional US image is recorded, transmitted and illustrated on the sonographer's monitor with a $20\,m\mathrm{sec}$ sampling time. The images of the remote environment are also captured online and shown to the sonographer. In another monitor, the interaction forces and the master and slave positions are plotted online for the sonographer (Fig. 3).
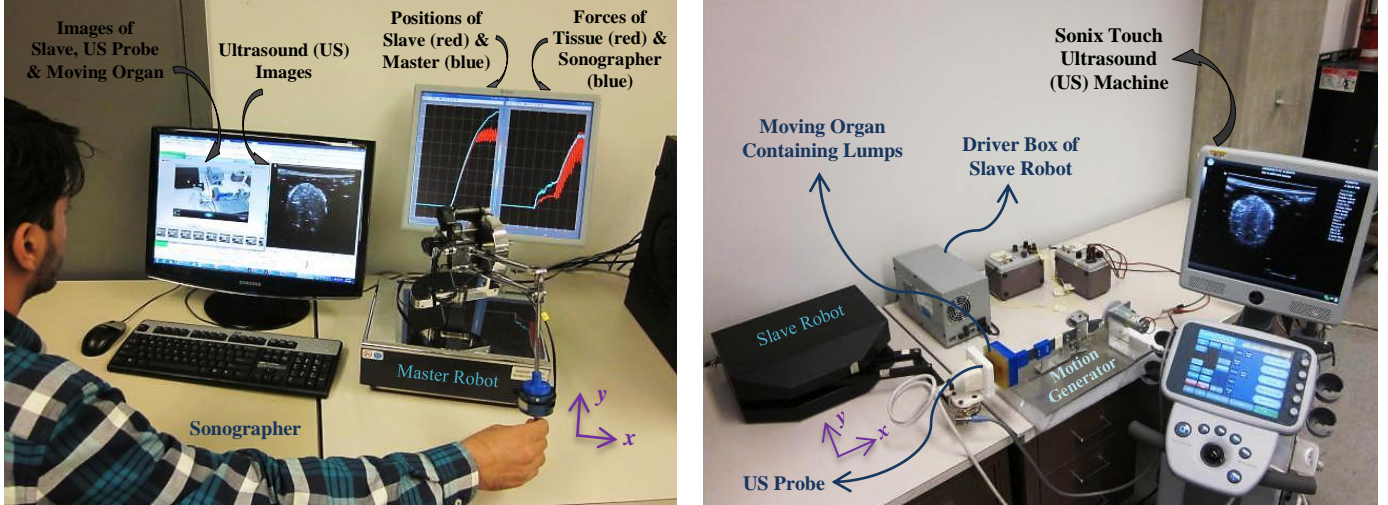
Fig. 3. The experimental setup for the tele-echography of moving organs, including the master and slave robots, the US machine, the motion simulator device. The left monitor is for on-line displaying the US images and the camera images of the remote slave site and the right monitor is for showing the interaction forces and the master and slave positions to the sonographer in the local site.

5.2. Soft Moving Organ and its Motion Generator

A motorized motion generator device (shown in Fig. 4) is designed and used to simulate the natural motion and force of the moving organ (or tissue) with an adjustable rate from high frequencies (such as the heart-beating) to lower ones (such as breathing). The position of this motion simulator is measured by the LP-30FP potentiometer sensor (Midori America Corp., Fullerton, CA, USA). This device is equipped with a DC motor and a cam-follower set to generate translational oscillatory motion for the artificial soft tissue attached to the end rod. Small spherical lumps are designed and incorporated inside the soft phantom tissue (Fig. 4) to represent muscles, tumors, or other tissues of interest to be visualized within the heart, chest, or breast. Imaging these lumps through ultrasound can be used to assess the performance of the proposed system in terms of image acquisition capability.
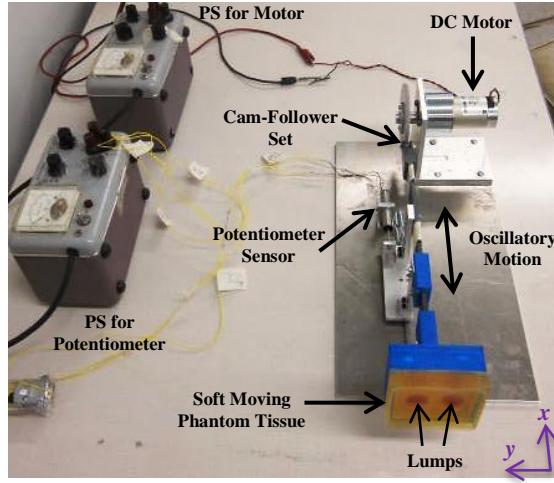

Fig. 4. The motorized motion generator device with the attached soft tissue containing small lumps.

The parameter values used in the control laws (11) and (12) and the adaptation laws (21) are listed in Table 1. These parameters are adjusted experimentally such that the tracking convergence performance is obtained appropriately (with suitable transient responses and small steady-state tracking errors). The "$\mathrm{sgn}(\varepsilon_s)$" function causes undesired discontinuities and chattering in the slave robot's control input (12); thus, the continuous function $\tanh(200\varepsilon_s)$ is employed in these experiments as an alternative to $\mathrm{sgn}(\varepsilon_s)$. The transmitted signals inside the communication channels (shown in Figs. 1 and 2) are considered to have $T_1 = 120\,m\mathrm{sec}$ and $T_2 = 120\,m\mathrm{sec}$ of time delays that are significant in common remote operations.

Table 1
Parameters of the control and adaptation laws used in the experimental studies.

Control	Adaptation
$\rho_{1,m} = 400$, $\rho_{2,m} = 450$, $\rho_{3,m} = 70$	
$\rho_{1,s} = 400$, $\rho_{2,s} = 450$, $\rho_{3,s} = 540$, $\rho_{4,s} = 1.8$	$\mathbf{W}_m = 2I$, $\mathbf{W}_s = 32I$

5.3. Moving Tissue with Heart Beating Frequency (High Freq.)

The US imaging of a beating-heart is important for intraoperative evaluations of its performance during its normal motion. For this purpose, the parameters of the slave (3) and the master (4) impedance models should be chosen based on the adjustment guidelines presented in Sec. 2.3 and Sec. 2.4, respectively. Accordingly, the employed impedance parameters and scaling factors in this experiment for the tele-echography of a moving tissue with heart-beating frequency are mentioned in Table 2 for both x and y directions of Cartesian space. Since the heart-beating frequency range is $\omega_{MT} \simeq 6.28 - 10.68$ rad/sec, the natural frequencies of the slave and master impedance models are set to $\omega_{n_s} = 50$ rad/sec and $\omega_{n_m} = 0.5$ rad/sec, respectively based on the discussions in Sec. 2.3 and Sec. 2.4.

Table 2
Parameters of the master and slave impedance models for ultrasound imaging of the moving tissue.

Master impedance parameters	Slave impedance parameters	Force and position scaling factors
$k_m = 8$ N/m	$k_s = 100$ N/m	$\eta_f = 1.5$
$c_m = 22.4$ N.s/m	$c_s = 2.8$ N.s/m	$\eta_p = 0.5$
$m_m = 32$ kg	$m_s = 0.04$ kg	

The positions of the master and slave impedance models responses ($\mathbf{x}_{imp_m}$ and $\mathbf{x}_{imp_s}$) with the master/sonographer and slave positions ($\mathbf{x}_m$ and $\mathbf{x}_s$) in x and y directions of Cartesian space are shown in Fig. 5.
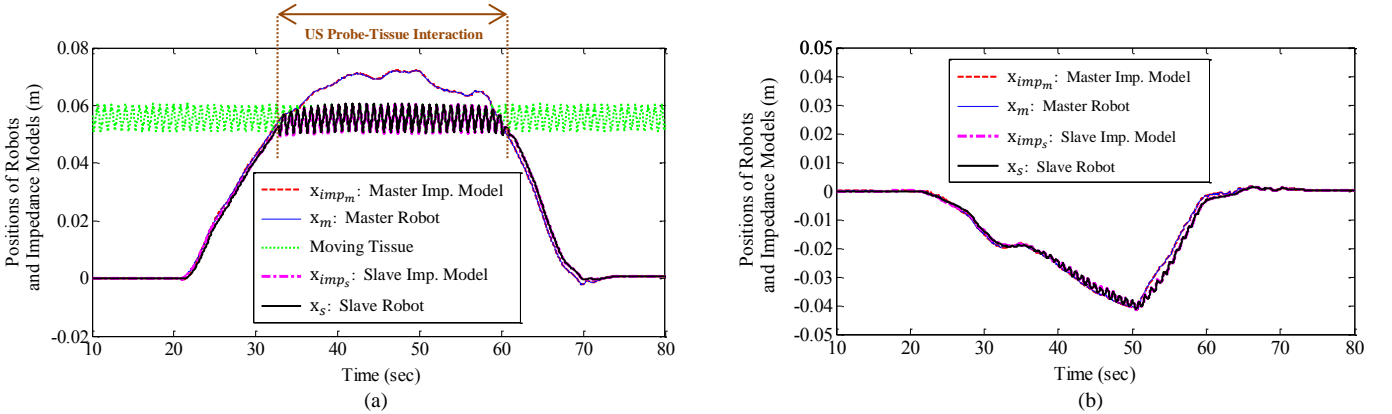

Fig. 5. Positions of the master and slave robots and their impedance models responses during US imaging of a moving tissue with heart-beating frequency: in (a) x and (b) y directions of Cartesian space.

As seen in Fig. 5, the master and slave robots' end-effectors track their corresponding impedance responses during the whole operation (before, after and during the moving tissue interaction) using the proposed nonlinear bilateral adaptive controller, as proved in Sec. 4. However, regarding the slave impedance model (3), after starting the US probe-tissue interaction and applying the tissue force $\mathbf{f}_{tis}$ to the slave robot, the slave has a flexibility and deviation $\tilde{\mathbf{x}}_{imp_s}$ with respect to the master trajectory.

Therefore, the slave robot has a fast compliance with the oscillatory tissue motion in response to the interaction force $\mathbf{f}_{tis}$ based on the adjusted characteristics of the impedance model (3), as discussed before in Sec. 2. Since the slave robot approaches and applies normal palpation forces to the tissue in the x direction of Cartesian space and the tissue motion is mostly in this direction (see Figs. 3 and 4), the slave deviation in the x direction (Fig. 5a) is higher than the one in the y direction (Fig. 5b). The sonographer also has a motion in the y direction to slide the US probe on the tissue surface in order to scan different sections of this phantom tissue (containing lumps).

To elaborate more on the convergence of tracking errors and the deviation of slave trajectory from the master's, these errors and deviation are plotted in Fig. 6.
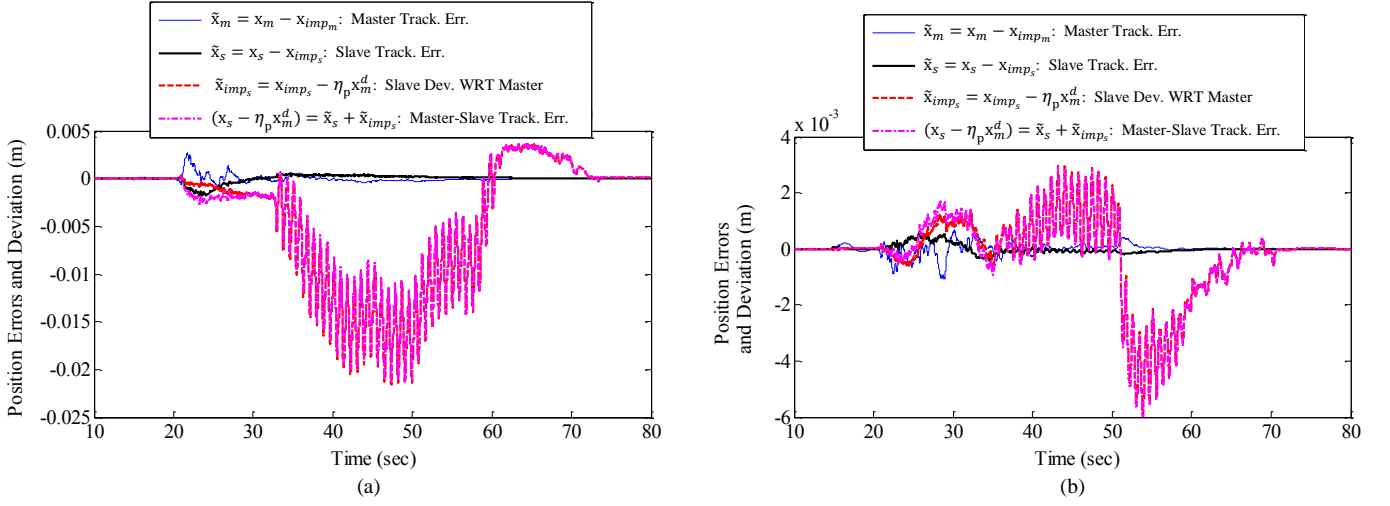

Fig. 6. Position tracking errors and slave deviation during US imaging of a moving tissue with heart-beating frequency: (a) in x direction and (b) in y direction.

The scaled-up applied interaction force from the slave robot to the moving tissue ($\eta_{f}\mathbf{f}_{tis}$) together with the applied interaction force from the sonographer hand to the master robot ($\mathbf{f}_{son}$) are demonstrated in Fig. 7. As shown in Fig. 7, after starting the interaction, the oscillatory force of the moving tissue is applied to the slave (Fig. 7) and causes the deviation of the slave trajectory from the master one (Figs. 5 and 6). It is seen that the US probe-tissue interaction force in the y (sliding) direction (Fig. 7b), which is mostly caused by friction, is significantly smaller than the interaction force in the x (palpation) direction (Fig. 7a), which is perpendicular to the tissue surface. Note that ultrasound gel is utilized between the US probe and the tissue surface, which reduces the friction and makes the interaction force in the y (sliding) direction small. As a result, the slave position deviation in the y direction (Fig. 6b) is considerably lower than the one in the x direction (Fig. 6a).
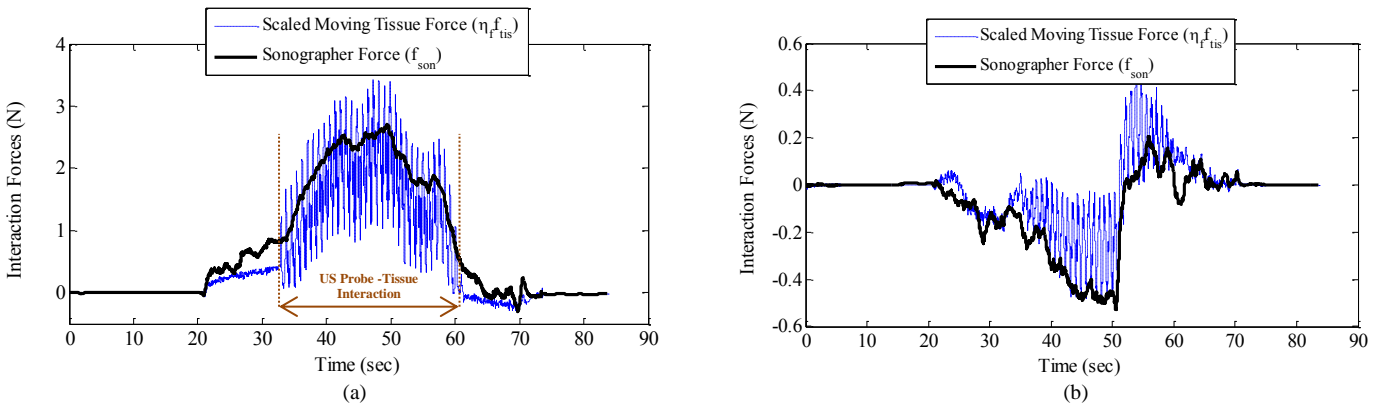

Fig. 7. Scaled tissue force (with $\eta_{f} = 1.5$) and the sonographer force during US imaging of a moving tissue with heart-beating frequency: (a) in x direction and (b) in y direction.

According to Fig. 7, as the applied interaction force $\mathbf{f}_{son}$ of the sonographer increases, the non-oscillatory value of the tissue force $\eta_{\mathrm{f}}\mathbf{f}_{tis}$ increases as well. In other words, the sonographer perceives the non-oscillatory (low-frequency) portion $\eta_{\mathrm{f}}\mathbf{f}_{tis_{LF}}$ of the moving tissue force as the haptic feedback, and its oscillatory (high-frequency) portion $\mathbf{f}_{tis_{HF}}$ is filtered. This performance is the result of adjustment of the master impedance model (4) described in Sec. 2.4. Thus, the force reflection performance is approximately achieved as $\mathbf{f}_{son} \rightarrow \eta_{\mathrm{f}}\mathbf{f}_{tis_{LF}}$, and the surgeon's feeling is similar to the stationary echography (US imaging) operation on the tissue (such as an arrested heart).

The trajectory of the slave robot in two-dimensional $x-y$ plane with respect to the soft tissue (containing lumps) is shown in Fig. 8. Moreover, some of the US images provided online for the sonographer via his monitor are illustrated in Fig. 8 at different positions of the US probe during the scanning of a lump inside the moving tissue.
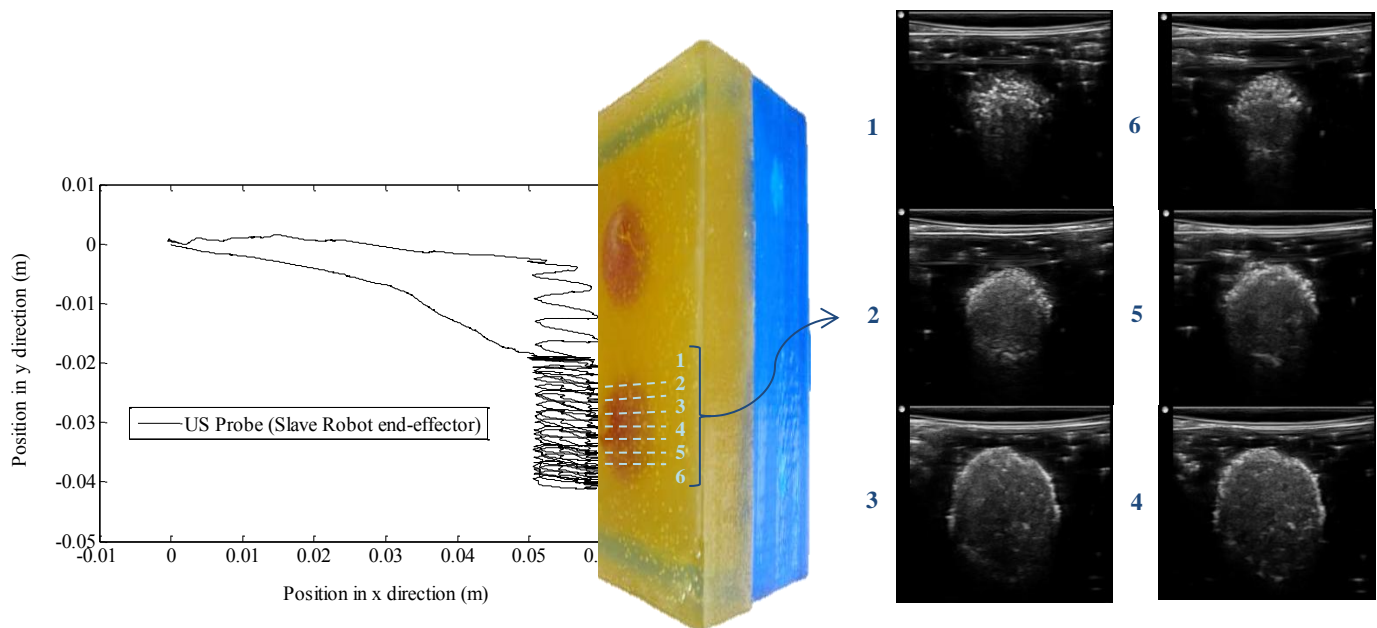

Fig. 8. The trajectory of the slave robot's end-effector in two-dimensional $x-y$ plane with respect to the soft tissue, and US images of some sections of the tissue containing lumps provided online for the sonographer.

5.4. Moving Tissue with Breathing Frequency (Low Freq.)

In this section, the experimental results for US imaging of a moving tissue with (low) breathing frequency are illustrated. This case occurs in US scanning of the patients' chest and/or breast during the normal breathing. For this purpose, two cases of adjustment of the impedance models are taken into account: The first one is when the impedance parameters are considered the same as in previous section presented in Table 2 for high-frequency moving tissue. Therefore, the natural frequency (or cut-off frequency) of the master impedance model (4), $\omega_{n_m} = 0.5$ rad/sec, is not much smaller than the low breathing frequency of the moving tissue $\omega_{MT} \simeq 0.2 - 0.5$ Hz $= 1.26 - 3.14$ rad/sec in comparison with the high beating frequency in Sec. 5.3. For this case, the position of the master and slave robots and their impedance models' responses in x direction are shown in Fig. 9a and the corresponding interaction forces are illustrated in Fig. 9b.
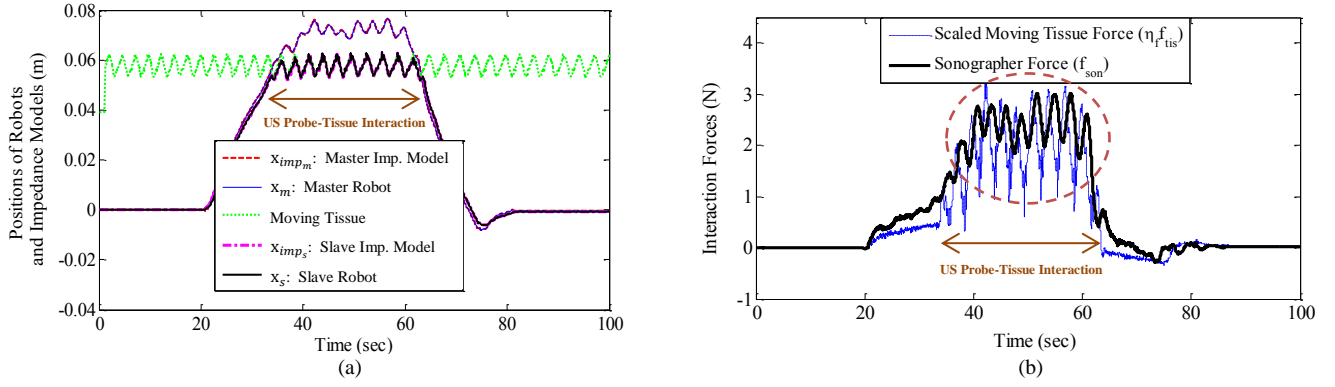
Fig. 9. (a) Position trajectories and (b) interaction forces in x direction , for US imaging of a moving tissue with breathing frequency, when $\omega_{n_m} = 0.5$ rad/sec .

As observed in Fig. 9, the oscillatory force of the moving tissue is not filtered well by the master impedance model and it is transferred to the sonographer's hand. This is due to the closeness of the natural frequency $\omega_{n_m} = 0.5$ rad/sec of the master impedance and the low (breathing) frequency $\omega_{MT} \simeq 2.3$ rad/sec of the tissue motion. In this case, the sonographer should overcome the oscillatory tissue force (Fig. 9b) in order to hold the master robot in a desired position (Fig. 9a) such that the slave robot remain in touch with the moving tissue via deviation from the master trajectory. If the sonographer does not overcome the oscillatory force and allow this tissue force to generate large oscillatory motions for the master robot, it may cause the slave robot/US's probe to detach from the moving tissue and the image quality to degrade. Note that perceiving oscillatory force is not much annoying for the sonographer in this case because of low frequency of this force.

In the next case of impedance adjustment with low breathing frequency, the master's natural frequency is considered to be $\omega_{n_m} = 0.2$ rad/sec that is less than half of the one used in the previous case. Accordingly, the parameters of the master impedance model (11) in Table 2 are changed to $c_m = 56$ N.s/m and $m_m = 200$ kg using the same stiffness $k_m = 8$ N/m and damping ratio $\zeta_m = 0.7$ as the previous section. The other parameters are the same as ones presented in Table 2. The positions and forces data for this case of US imaging is demonstrated in Fig. 10a and 10b, respectively.
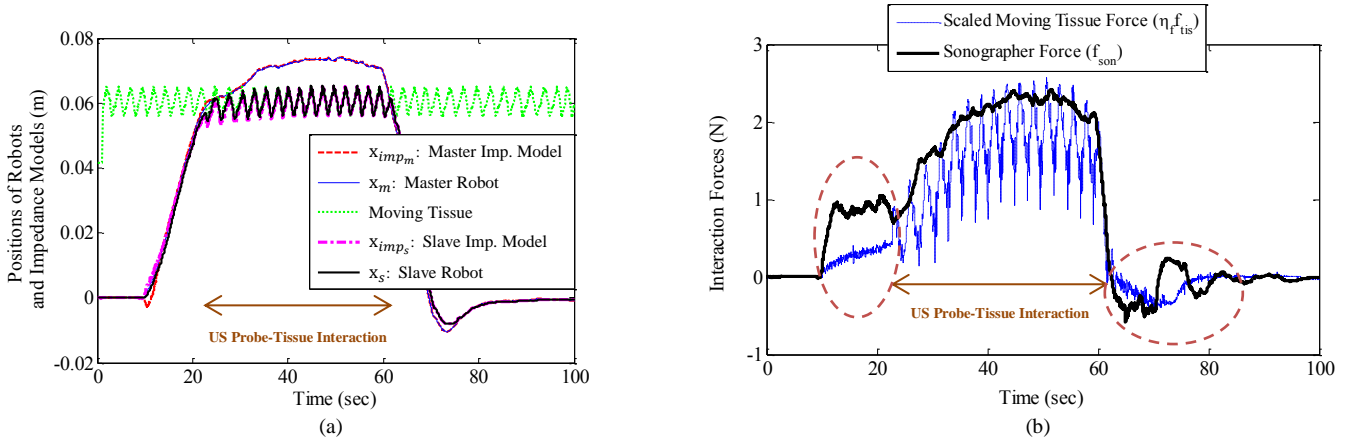

Fig. 10. (a) Position trajectories and (b) interaction forces in x direction, for US imaging of a moving tissue with breathing frequency, when $\omega_{n_m} = 0.2$ rad/sec .

According to Fig. 10, the oscillatory force of the moving tissue with breathing frequency is filtered and not transferred to the sonographer during the US probe-tissue interaction. However, in free motions before and after the tissue interaction, the master robot becomes more sluggish and requires larger sonographer's forces (Fig. 10b) in comparison with the previous case (Fig. 9b). This is due to the increase of the master damping and inertia (c_m and m_m) as a result of the decrease of master natural frequency to $\omega_{n_m} = 0.2$ rad/sec . Note that the natural frequency of the slave impedance model ($\omega_{n_s} = 50$ rad/sec) is the same as in the previous section and not required to be changed because it is sufficiently larger than the low breathing frequency

14

($\omega_{MT} \simeq 2.3$ rad/sec) of the tissue motion.

Based on the presented impedance adjustments for the master robot, the US scanning of a tissue having low frequency motion can be performed with two force reflection cases. In the first case with higher natural master frequency, the master robot can be moved easier in free space but the oscillatory force of the tissue is transferred to the sonographer's hand during the interaction. In the second case with smaller natural frequency, the master robot becomes slower and requires much more force for the movement, however, the oscillatory force of the tissue is filtered and not transferred to the sonographer.

6. Conclusion

A new impedance-based control strategy for the tele-echography (remote ultrasound imaging) of moving organs, using multi-DOF telerobotic systems subjected to time delays, was presented and experimentally evaluated. In this strategy, the slave robot holding the US probe has an adjustable flexibility with respect to the applied moving tissue force during tracking the master robot's trajectory. Accordingly, continuous contact between the US probe and the tissue was achieved during oscillatory motions of the organ, which is necessary to maintain the quality of the US images. On the other hand, the oscillatory portion of the moving tissue force can be filtered from the haptic force feedback to the sonographer's hand via the master robot. Therefore, the sonographer's feeling is similar to the direct US imaging of a stationary (arrested) organ; however, the slave robot has a compliance with the organ's motion during the operation. The proposed strategy can be used in the robot-assisted tele-echography of the beating-heart, moving chest and/or breast during the normal breathing for remote patients.

The mentioned performances were achieved by the appropriate adjustments of the two stable master and slave impedance models. Moreover, the trade-offs in choosing the master and slave impedance parameters were determined. The stability of the telerobotic system and the tracking convergence to the impedance models' responses were provided in the presence of communication delays and modeling uncertainties, as proved via the Lyapunov stability theorem and evaluated experimentally.

The experimental results were presented for the US imaging of a simulated moving organ with beating heart (high) and also breathing chest (low) motion frequencies. The presented theory and experiments indicated the capability of this method to be employed in the future patient studies. Due to the stability, robustness and tracking features, the patient safety in the remote site is significantly improved during the interaction with the US probe.

Acknowledgements

References

[1] Okamura AM. Methods for haptic feedback in teleoperated robot-assisted surgery. Industrial Robot: An International Journal 2004; 31: 499-08.

[2] Lee SJ, Lee SC, Ahn HS. Design and control of tele-matched surgery robot. Mechatronics 2014; 24: 395-06.

[3] Carignan CR, Krebs HI. Telerehabilitation robotics: Bright lights, big future. Journal of Rehabilitation Research and Development 2006; 43: 695-10.

[4] Meng W, Liu Q, Zhou Z, Ai Q, Sheng B, Xie S, Recent development of mechanisms and control strategies for robot-assisted lower limb rehabilitation. Mechatronics 2015; 31: 132-45.

[5] Najafi F, Sepehri N. Design and Prototyping of a Force-Reflecting Hand-Controller for Ultrasound Imaging. Journal of Mechanisms and Robotics 2011; 3: 021002 (11 pages).

[6] Najafi F, Sepehri N. A novel hand-controller for remote ultrasound imaging. Mechatronics 2008; 18: 578-90.

[7] Kim C, Chang D, Petrisor D, Chirikjian G, Han M, Stoianovici D. Ultrasound Probe and Needle-Guide Calibration for Robotic Ultrasound Scanning and Needle Targeting. IEEE Transactions on Biomedical Engineering 2013; 60: 1728-34.

[8] Schneider C, Nguan C, Rohling R, Salcudean S. Tracked "Pick-Up" Ultrasound for Robot-Assisted Minimally Invasive Surgery. IEEE Transactions on Biomedical Engineering 2016; 63: 260-68.

[9] Bell MAL, Sen HT, Iordachita I, Kazanides P. Force-controlled ultrasound robot for consistent tissue pre-loading: Implications for acoustic radiation force elasticity imaging. In: IEEE RAS & EMBS International Conference on Biomedical Robotics and Biomechatronics. IEEE; 2014. p. 259-64.

[10] Bell MAL, Kumar S, Kuo L, Sen HT, Iordachita I, Kazanides P. Toward standardized acoustic radiation force-based ultrasound elasticity measurements with robotic force control. IEEE Transactions on Biomedical Engineering 2016; 63: 1517-24.

[11] Vilchis A, Troccaz J, Cinquin P, Masuda K, Pellissier F. A new robot architecture for tele-echography. IEEE Transactions on Robotics and Automation 2003; 19: 922-26.

[12] Sengupta PP, Narula N, Modesto K, Doukky R, Doherty S, Soble J, Narula J. Feasibility of Intercity and Trans-Atlantic Telerobotic Remote Ultrasound: Assessment Facilitated by a Nondedicated Bandwidth Connection. JACC: Cardiovascular Imaging 2014; 7: 804-09.

[13] Sen HT, Bell MAL, Iordachita I, Wong J, Kazanides P. A cooperatively controlled robot for ultrasound monitoring of radiation therapy. In: IEEE/RSJ International Conference on Intelligent Robots and Systems (IROS). IEEE; 2013. p. 3071-76.

[14] Koizumi N, Warisawa S, Nagoshi M, Hashizume H, Mitsuishi M. Construction Methodology for a Remote Ultrasound Diagnostic System. IEEE Transactions on Robotics 2009; 25: 522-38.

[15] Santos L, Cortesao R. Admittance control for robotic-assisted tele-echography. In: International Conference on Advanced Robotics (ICAR). IEEE; 2013. p. 1-7.

[16] Monfaredi R, Wilson E, Azizi koutenaei B, Labrecque B, Leroy K, Goldie J, Louis E, Swerdlow D, Cleary K. Robot-assisted ultrasound imaging: Overview and development of a parallel telerobotic system. Minimally Invasive Therapy & Allied Technologies 2015; 24: 54-62.

[17] Schlosser J, Salisbury K, Hristov D. Telerobotic system concept for real-time soft-tissue imaging during radiotherapy beam delivery. Medical Physics 2010; 37: 6357-67.

[18] Zandsteeg CJ, Bruijnen DJH, Van de Molengraft MJG. Haptic tele-operation system control design for the ultrasound task: A loop-shaping approach. Mechatronics 2010; 20: 767-77.

[19] Reed GL, Singer DE, Picard EH, DeSanctis RW. Stroke Following Coronary-Artery Bypass Surgery. New England Journal of Medicine 1988; 319: 1246-50.

[20] Newman MF, Kirchner JL, Phillips-Bute B, Gaver V, Grocott H, Jones RH, Mark DB, Reves JG, Blumenthal JA. Longitudinal Assessment of Neurocognitive Function after Coronary-Artery Bypass Surgery. New England Journal of Medicine 2001; 344: 395-02.

[21] Kettler DT, Plowes RD, Novotny PM, Vasilyev NV, Del Nido PJ, Howe RD. An active motion compensation instrument for beating heart mitral valve surgery. In: IEEE/RSJ International Conference on Intelligent Robots and Systems (IROS). IEEE; 2007. p. 1290-95.

[22] Tavakoli M, Patel RV, Moallem M, Aziminejad A. Haptics For Teleoperated Surgical Robotic Systems. NJ, World Scientific Publishing Co.; 2008.

[23] Liu YC, Chopra N. Control of semi-autonomous teleoperation system with time delays. Automatica 2013; 49: 1553-65.

[24] Liu X, Tao R, Tavakoli M, Adaptive control of uncertain nonlinear teleoperation systems. Mechatronics 2014; 24: 66-78.

[25] Hashemzadeh F, Sharifi M, Tavakoli M. Nonlinear trilateral teleoperation stability analysis subjected to time-varying delays. Control Engineering Practice 2016; 56: 123-35.

[26] Cho HC, Park JH. Stable bilateral teleoperation under a time delay using a robust impedance control. Mechatronics 2005; 15: 611-25.

[27] Ginhoux R, Gangloff J, de Mathelin M, Soler L, Sanchez MMA, Marescaux J. Active filtering of physiological motion in robotized surgery using predictive control. IEEE Transactions on Robotics 2005; 21: 67-79.

[28] Bebek O, Cavusoglu MC. Intelligent Control Algorithms for Robotic-Assisted Beating Heart Surgery. IEEE Transactions on Robotics 2007; 23: 468-80.

[29] Bachta W, Renaud P, Laroche E, Forgione A, Gangloff J. Active Stabilization for Robotized Beating Heart Surgery. IEEE Transactions on Robotics 2011; 27: 757-68.

[30] Bowthorpe M, Tavakoli M, Becher H, Howe R. Smith Predictor-Based Robot Control for Ultrasound-Guided Teleoperated Beating-Heart Surgery. IEEE Journal of Biomedical and Health Informatics 2014; 18: 157-66.

[31] Bowthorpe M, Tavakoli M. Physiological Organ Motion Prediction and Compensation Based on Multi-rate, Delayed, and Unregistered Measurements in Robot-assisted Surgery and Therapy. IEEE/ASME Transactions on Mechatronics 2016; 21: 900-11.

[32] Nakamura Y, Kishi K, Kawakami H. Heartbeat synchronization for robotic cardiac surgery. In: IEEE International Conference on Robotics and Automation (ICRA). IEEE; 2001. p. 2014-19.

[33] Wagner CR, Stylopoulos N, Jackson PG, Howe RD. The Benefit of Force Feedback in Surgery: Examination of Blunt Dissection. Presence: Teleoperators and Virtual Environments 2007; 16: 252-62.

[34] Zarrouk Z, Chemori A, Poignet P. Force feedback control for compensation of physiological motions in beating heart surgery with real-time experiments. In: International Conference on Systems and Control (ICSC). 2013. p. 956-61.

[35] Cagneau B, Zemiti N, Bellot D, Morel G. Physiological Motion Compensation in Robotized Surgery using Force Feedback Control. In: IEEE International Conference on Robotics and Automation (ICRA). IEEE; 2007. p. 1881-86.

[36] Moreira P, Liu C, Zemiti N, Poignet P. Beating Heart Motion Compensation Using Active Observers and Disturbance Estimation. In: IFAC Symposium on Robot Control (SYROCO). IFAC; 2012. p. 741-46.

[37] Dominici M, Poignet P, Dombre E. Compensation of physiological motion using linear predictive force control. In: IEEE/RSJ International Conference on Intelligent Robots and Systems (IROS). IEEE; 2008. p. 1173-78.

[38] Dominici M, Cortesao R, Sousa C. Heart motion compensation for robotic-assisted surgery predictive approach vs. active observer. In: IEEE International Conference on Robotics and Automation (ICRA). IEEE; 2011. p. 6252-57.

[39] Dominici M, Cortesão R. Cascade force control for autonomous beating heart motion compensation. Control Engineering Practice 2015; 37: 80-88.

[40] Kesner SB, Howe RD. Robotic catheter cardiac ablation combining ultrasound guidance and force control. International Journal of Robotics Research 2014; 33: 631-44.

[41] Yuen SG, Perrin DP, Vasilyev NV, del Nido PJ, Howe RD. Force tracking with feed-forward motion estimation for beating heart surgery. IEEE Transactions on Robotics 2010; 26: 888-96.

[42] Sharifi M, Behzadipour S, Vossoughi G. Nonlinear model reference adaptive impedance control for human–robot interactions. Control Engineering Practice 2014; 32: 9-27.

[43] Slotine JJE, Li W. Applied nonlinear control. NJ, Englewood Cliffs: Prantice-Hall; 1991.

[44] Sharifi M, Behzadipour S, Vossoughi GR. Model reference adaptive impedance control in Cartesian coordinates for physical human–robot interaction. Advanced Robotics 2014; 28: 1277-90.

[45] Liu X, Tavakoli M. Adaptive Control of Teleoperation Systems With Linearly and Nonlinearly Parameterized Dynamic Uncertainties. Journal of Dynamic Systems, Measurement, and Control 2012; 134: 021015 (10 pages).

[46] Çavuşoğlu MC, Feygin D, Tendick F. A Critical Study of the Mechanical and Electrical Properties of the PHANToM Haptic Interface and Improvements for High-Performance Control. Presence: Teleoperators & Virtual Environments 2002; 11: 555-68.

[47] Dyck MD. Measuring the Dynamic Impedance of the Human Arm. M.Sc. Thesis, Department of Electrical and Computer Engineering, University of Alberta. 2013.

[48] Dyck M, Tavakoli M. Measuring the dynamic impedance of the human arm without a force sensor. In: IEEE International Conference on Rehabilitation Robotics (ICORR). IEEE; 2013. p. 1-8.